Additive Manufacturing 57 (2022) 102958

Contents lists available at ScienceDirect

Additive Manufacturing

journal homepage: www.elsevier.com/locate/addma

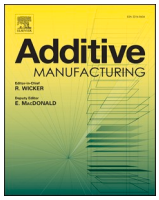

Research Paper

Controlling the columnar-to-equiaxed transition during Directed Energy Deposition of Inconel 625

S. Li [a,b], J.Y. Li [a,b], Z.W. Jiang [a,b], Y. Cheng [c], Y.Z. Li [d], S. Tang [a,b], J.Z. Leng [e], H.X. Chen [f], Y. Zou [f], Y.H. Zhao [b,g], J.P. Oliveira [h,i,*,1], Y. Zhang [a,b,**], K.H. Wang [b]

[a] Herbert Gleiter Institute of Nanoscience, Nanjing University of Science and Technology, Nanjing 210094, China
[b] School of Materials Science and Engineering, Nanjing University of Science and Technology, Nanjing 210094, China
[c] Nanjing Enigma Automation Corporation, LTD, Nanjing 211153, China
[d] School of Physical Science and Technology, Northwestern Polytechnical University, Xi'an 710072, China
[e] Department of Mechanical Engineering, McGill University, Montreal, QC H3A 0C3, Canada
[f] Department of Materials Science & Engineering, University of Toronto, Toronto, ON M5S 3E4, Canada
[g] Nano and Heterogeneous Materials Center, Nanjing University of Science and Technology, Nanjing 210094, China
[h] UNIDEMI, Department of Mechanical and Industrial Engineering, NOVA School of Science and Technology, Universidade NOVA de Lisboa, Caparica 2829-516, Portugal
[i] CENIMAT/I3N, Department of Materials Science, NOVA School of Science and Technology, Universidade NOVA de Lisboa, 2829-516 Caparica, Portugal

ARTICLE INFO

Keywords:
Inconel 625
Additive Manufacturing
Microstructure
Texture
Mechanical Properties

ABSTRACT

In this work, the grain orientation and mechanical properties of Inconel 625 are tailored by varying the process parameters during directed energy deposition. Under the same deposition speed, increasing the current is effective in promoting the columnar-to-equiaxed transition due to modifications on the thermal cycle. The solidification conditions (temperature gradient and cooling rate) were characterized during the process. A comparison with an existing solidification map for Inconel 625 indicates that the temperature gradients in the melt pool of the sample fabricated with larger current decrease sufficiently to permit the nucleation and growth of equiaxed grains. Uniaxial tensile testing showed that the sample with equiaxed grain microstructure exhibits a higher yield strength (increase by 36 %) when compared to the sample with columnar grains. Contributions of various strengthening mechanisms to the yield strength are quantified in terms of grain boundary strengthening, dislocation strengthening, and solid-solution strengthening. It is found that the higher yield strength of samples that possess equiaxed grains can be attributed to the enhanced dislocation strengthening arising from the large average Taylor factor.

1. Introduction

Additive Manufacturing (AM) comprises a set of processing technologies, which possess high economical advantage over conventionally used manufacturing methods. Components with complex shapes that are not achievable by conventional manufacturing techniques can be realized via AM [1–3]. This advantage has aroused great interest in applying AM to commercial alloys currently used in several applications, such as those of the biomedical, automotive and aerospace industries [4–8]. Inconel 625, which was used in this research, is a commercial alloy with a wide range of applications, especially in the aerospace and oil & gas fields. This material combines excellent tensile and creep strengths with extraordinary oxidation resistance and high-temperature corrosion resistance [9,10]. AM is expected to solve the problems of conventional manufacturing methods related to processing limitations, material waste and high processing costs associated with components that possess

* Corresponding author at: UNIDEMI, Department of Mechanical and Industrial Engineering, NOVA School of Science and Technology, Universidade NOVA de Lisboa, Caparica 2829-516, Portugal.
** Corresponding author at: Herbert Gleiter Institute of Nanoscience, Nanjing University of Science and Technology, Nanjing 210094, China.
E-mail addresses: jp.oliveira@fct.unl.pt (J.P. Oliveira), yong@njust.edu.cn (Y. Zhang).

[1] Statement on Conflicts of Interest: One of the authors of this article is part of the Editorial Board of the journal. To avoid potential conflicts of interest, the responsibility for the editorial and peer-review process of this article lies with the journal's other editors. Furthermore, the authors of this article were removed from the peer review process and had no, and will not have any access to confidential information related to the editorial process of this article.

https://doi.org/10.1016/j.addma.2022.102958
Received 6 January 2022; Received in revised form 27 May 2022; Accepted 5 June 2022
Available online 8 June 2022

complex shapes [11–13]. However, the overarching challenge in AM is to tailor the microstructure of Inconel 625 while maintaining material properties that meet the standards for use of these materials in the challenging environments encountered in energy, space and nuclear applications.

Due to the small melt pool and steep temperature gradient ahead of the solid-liquid interface featured by Powder Bed Fusion (PBF) methods, it is known that Inconel 625 tends to solidify in an epitaxial manner, leading to the generation of columnar-like grains with <001> crystal direction oriented along the build direction [14,15]. Similar observations were also reported for other types of Inconel alloys, such as Inconel 718 [16,17]. Generally, the columnar grains that are oriented along the loading direction can offer superior mechanical properties of parts at high temperatures. The intrinsic columnar structure will render anisotropy mechanical properties in the fabricated components which can be a setback for its use in applications where multiaxial loading conditions are found. Moreover, it may also increase the probability for the occurrence of hot tearing under multi-directional high temperature loading conditions [18,19].

Several different strategies have recently been pursued for promoting the Columnar-to-Equiaxed Transition (CET) during AM [20]. One approach for promoting the CET is to utilize high-intensity ultrasounds to promote the vibration of the melt and therefore, enhancing the grain nucleation upon solidification, which was recently proved efficient to enable the formation of equiaxed grain structures in laser-based Directed Energy Deposition (DED) of Ti-6Al-4 V and Inconel 625 [20]. Ti(O, N) particles can also be used to trigger the CET in Fe-Ti alloys during laser powder bed fusion [21], thus enhancing the material mechanical properties. Intrinsically, manipulation of the AM processing parameters to control the temperature gradient (G_L), solidification rate/velocity (R_L) of the solid-liquid interface, and cooling rate (C_L) has the potential to enable the formation of equiaxed grain structures [22,23]. Raghavan et al. [22] demonstrated that increasing the preheating temperature, beam current, and/or time on spot promotes the CET in Inconel 718 during electron beam additive manufacturing which was attributed to a reduction in G_L.

According to the G_L vs. R_L plots established for the Inconel 625 alloy, the formation of equiaxed grains could be enabled by reducing the G_L to below $< 10^5$ K/m, which is one or two orders of magnitude lower than that of typically obtained during PBF [24]. Bontha et al. [25] modelled the grain structure of a Ti-6Al-4 V alloy during AM, and found that the small scale deposition conditions will yield temperature gradients well above 10^6 K/m and solidification rates of the order of 0.1 cm/s, leading to the formation of fully columnar grain structures. However, the temperature gradients are remarkably reduced by more than one order of magnitude ($<10^5$ K/m) when larger scale (higher power) AM processes were modelled, and it was predicted that equiaxed-like grained microstructures could occur. The scale and characteristics of Wire Arc Additive Manufacturing (WAAM) might offer a thermal environment satisfying the required solidification conditions for the nucleation of equiaxed grains. Compared to PBF processes, WAAM, as a part of DED processes, shows advantages of high deposition rate, high energy efficiency and low capital costs [26–29]. Moreover, WAAM heat sources have the characteristics of low heat flux density, large heating radius and high heat source intensity. The high specific energy combined with high material deposition rate creates deeper and larger melt pools [22,30–34], which allows the solidifying materials to experience high temperatures for a prolonged period of time [35]. Correspondingly, a smaller G_L, which facilitates the formation of equiaxed grains and subsequent growth, could be achieved in the large melt pool during WAAM. Furthermore, Dinovitzer et al. [30] investigated the effects of processing parameters, such as traveling speed of the welding torch and current, on the melt pool depth during WAAM, and found out that the decrease of the travel speed or increase of the current promoted an increase on the melt pool depth. This indicates that proper selection of the processing parameters may tailor the geometry of the melt pool to obtained desirable grain structures during WAAM, though the available cases of CET achieved in WAAM samples are mostly achieved by the addition of particles as the grain refiners [36,37].

Table 1
Chemical composition of Inconel 625 (wt%).

Ni	Cr	Mo	Nb	Fe	Ti	C	Mn	Si
Bal.	22.13	9.16	3.63	0.34	0.13	0.06	0.05	0.22

WAAM of Inconel 625 alloy is already well-established for the creation parts with a single parameter set [36,37]. For example, Ravi et al. revealed that the microstructure in WAMMed Inconel 625 is characterized by the presence of a columnar dendritic accompanied with carbides [37]. However, it is still not clear that whether processing parameters can influence the grain structures in terms of grain size, orientation, morphology, and mechanical properties.

Therefore, the aim for present work is to develop an experimental design methodology to tailor the geometry of the melt pool by tunning the linear energy density to achieve the regulation of grain structures within the melt pool. The Linear Energy Density is influenced by the processing parameters as described below [38]:

$$LED = \frac{V \times I}{V_t} \times \eta_u \tag{1}$$

where V is the voltage (V) and I is the current (A), V_t is the traveling speed of the welding torch (mm/s). η_u is the process efficiency, which is close to 0.9 for CMT [39]. We intended to minimize the number of processing parameters to be varied, avoiding any interactions between processing parameters. First, the traveling speed is fixed, as it is independent of the CMT Advance 4000 power source. Due to the characteristic of power source used, the current was increased by finely tunning the wire feeding speed, while the voltage remained constant. Therefore, the current is the sole parameter modified to vary the LED,

Fig. 1. Main components of CMT-WAAM system.

Table 2
Processing parameters used to build WAAM parts.

Traveling speed (mm/s)	Feeding speed (m/min)	Current (A)	Voltage (V)	LED (J/mm)
10	4.1	104	13.4	125
10	4.6	116	13.4	140

and subsequently explore whether the control of LED during WAAM can affect the solidification conditions ahead of the solid-liquid interface and consequently enable the formation of equiaxed grain structures in the WAAM-fabricated Inconel 625 alloy. The uniaxial tensile properties of Inconel 625 alloy fabricated using WAAM with different processing conditions were determined and the correlation with the material microstructure features was rationalized in terms of grain boundary strengthening, solid solution strengthening and dislocation strengthening. These findings could serve as a valuable reference for the fabrication of Inconel 625 parts with tailored grain morphology, texture, and mechanical properties.

2. Materials and method

2.1. Materials and processing

The wire feedstock selected for this study was a 1.2 mm diameter metal wire, made of the commercial Inconel 625. The chemical composition of wire was measured by means of SPECTRO MAXx optical emission spectroscopy (OES), as listed in Table 1. The additive manufacturing test adopts the WAAM manufacturing system based on Cold Metal Transfer (CMT). CMT is known for the ability to reduce the heat input compared to other arc-based processes, thus imposing less several thermal cycles to the material being deposited. The system mainly consists of six-axis Fanuc robot arm, Fronius CMT Advanced 4000 welding machine, computer slicing simulation software (*Lungopnt*) system, wire feeding system (Fig. 1). The trim length for the present WAAM processing is 15 mm. A carbon steel Q235, with a thickness of 30 mm, was used as the substrate. The substrate surface was polished with sandpaper and then the surface oxide film was removed by laser cleaning. Finally, the substrate was wiped and cleaned by alcohol prior to the WAAM depositions.

The deposited samples are cylinders with dimensions of Ø 50 mm × 100 mm. In this study, two sets of different deposition parameters were used to fabricate the cylindrical samples. The specific manufacturing parameters are shown in Table 2. According to the Eq. (1), the main variable is the electric current. The increase of current promotes an enhancement on the LED. The deposition strategy used is shown in Fig. 2. After each layer is deposited, the welding gun is lifted by 1.8 mm. During the deposition process, the deposition path is rotated 90° for each subsequent layer, and there is no interlayer waiting time. To avoid oxidation, 70 % Ar + 30 % He shielding gas at a flow rate of 18 L/min was used during the process.

2.2. Microstructure and mechanical characterization

The samples for microstructural and mechanical characterization were extracted by wire Electrical Discharge Machining (EDM). The deposited samples were sequentially grounded using 240, 400, 600, 800, and 1200 grit SiC sandpapers. Then, the samples were sequentially polished with a diamond grinding paste with sizes of 1 and 0.5 μm. In order to further reduce the surface roughness of the samples, the mechanically polished samples were placed in a 10 % perchloric acid and 90 % alcohol solution for electrolytic polishing at a voltage of 14 V. Then, the as-deposited microstructure and element distribution were analysed with a Carl Zeiss AG Scanning Electron Microscope (SEM) equipped with an Electron Backscatter Diffraction (EBSD) unit and Energy Dispersive Spectrometer (EDS). The working distance and acceleration voltage for the EBSD measurements are 12–16 mm and 20 kV. The tilt angle for the EBSD measurement is 70°. The step sizes of EBSD

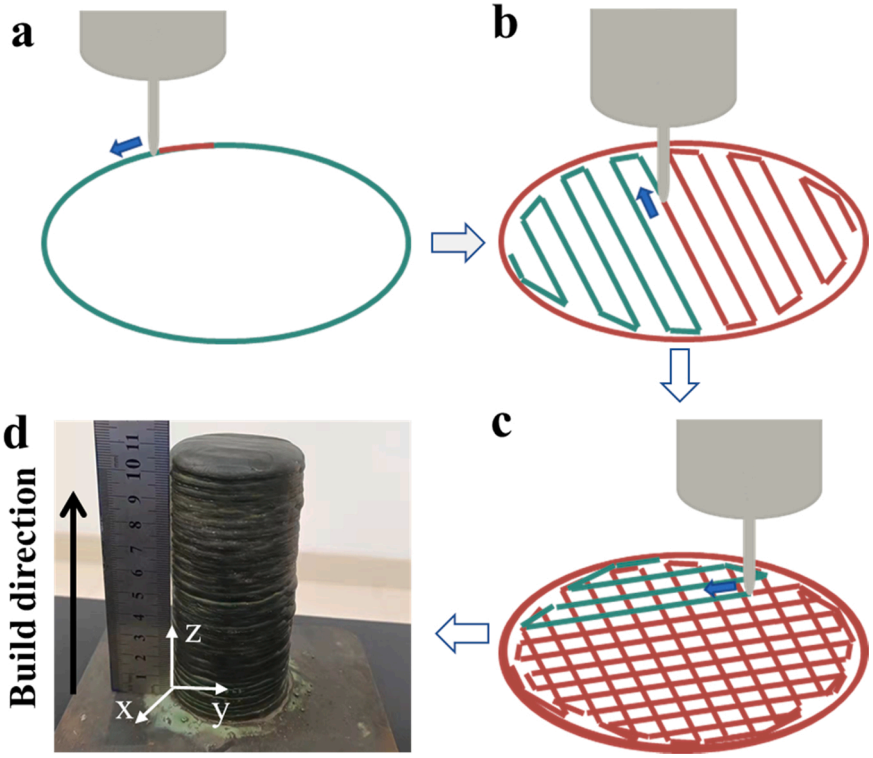

Fig. 2. (a–c) Illustration of the WAAM scanning strategy and the build direction. The red line indicates the track that has been printed and the arrow indicates the moving direction of the arc; (d) WAAM - fabricated sample with substrate. (For interpretation of the references to colour in this figure legend, the reader is referred to the web version of this article.)

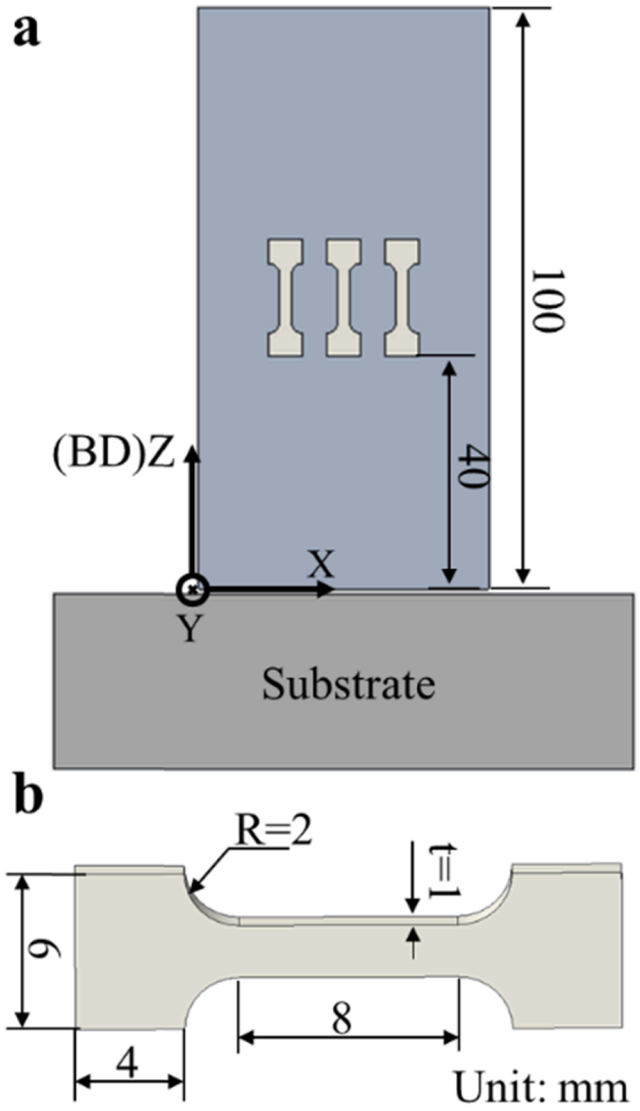

Fig. 3. (a) Extracted position and (b) dimensions of tensile specimens in the cylinder WAAM-processed Inconel 625 alloy.

measurements for grain size and Kernel Average Misorientation (KAM) are 10 and 0.7 μm, respectively. The working distance and acceleration voltage for the EDS measurements are 6 mm and 20 kV. For Optical Microscopy (OM) observations, the samples were etched using a solution of 15 ml HCl, 10 ml HNO_3 and 10 ml CH_3COOH, with a dwell time of 8 s. The morphology of the melt pool and the evolution of the microstructure were characterized by a Leica CTR6 optical microscope. The crystal structure of the samples was further evaluated by X-Ray Diffraction (XRD) using Cu radiation operating at 40 kV and 40 mA. All samples were scanned in the standard geometry from 20° to 120° for 2θ with a step size 0.02° and a dwell time of 0.6 s per step. A FEI Tecnai 20 Transmission Electron Microscope (TEM) was used to examine the secondary phase particles and dislocations in the WAAM deposits.

Samples for tensile testing were obtained at the same position from the two WAAM-deposited cylinders by wire EDM. The specimens for tensile tests had a gauge length of 8 mm, width of 2 mm and thickness of 1 mm. The orientation and dimensions of the tensile test samples are shown in Fig. 3. The tensile tests were carried out on an Instron 5982 tensile test instrument, equipped with a digital image correlation system to accurately measure strain. The tensile tests were performed at a tensile rate of 3×10^{-4} s^{-1}, along the Build Direction (BD) of the WAAM-fabricated cylindrical samples, and at room temperature.

3. Results

3.1. Microstructure and crystallographic texture

The EBSD orientation maps along the *Z*-axis of melt pools at the top layer in the columnar and equiaxed samples observed on the *X-Z* plane are shown in Fig. 4a and d, while the corresponding EBSD orientation maps along the *X*-axis are shown in Fig. 5a and d. The white dashed lines in Fig. 4a and d outlined the melt boundaries. It is evident that the crystallographic texture, grain structure and growth directions are remarkably different in the melt pools of two above mentioned samples. EBSD analysis indicated that the microstructure of the two fabricated samples is characterized by columnar grains and equiaxed grains microstructures, respectively (see Figs. 4 and 5). Therefore, the two samples are hereafter denoted as the columnar sample (LED 125 J/mm) and equiaxed sample (LED 140 J/mm), respectively. Within the melt pools at the top layer of the columnar sample (see Figs. 4a and 5a), grains tend to grow straight traversing multiple deposited layers along the build direction. The majority of the columnar grains exhibit a <001> crystal orientation along the build direction (*Z*-axis). However, in the equiaxed sample (see Figs. 4d and 5d), the grains grow perpendicular to the melt pool boundary, similar to earlier observations in laser powder-bed fusion of metallic alloys with cubic structure [40]. The crystal orientation map along *Z*-axis of Fig. 4d indicates that the <001> texture was significantly weakened as compared to the columnar sample. Furthermore, it is also noted that the growth of grains in the equiaxed sample was usually interrupted within the melt pools, leading to a more equiaxed grain morphology. Statistical measurements show that the columnar grains in the columnar sample have typically several millimetres in length and 354 ± 65 μm in width. The equiaxed sample shows a grain structure with an average length of 550 ± 430 μm and width of 248 ± 28 μm. The significantly reduced grain aspect ratio, i.e., ~7.62 for columnar sample vs. ~3.36 for the equiaxed sample, indicates the strong tendency for CET to occur within the melt pools at the top layer in equiaxed sample. Representative crystal orientation maps and Inverse Pole Figures (IPFs) along build direction obtained on the area for tensile specimens in columnar and equiaxed samples are displayed in Fig. 4b-c and e-f, respectively, while the corresponding crystal orientation maps and IPFs along the *X*-axis are shown in Fig. 5b-c and e-f. The overall height of the columnar sample in the building direction is about 100 mm, and the position for extracting tensile samples is 40–80 mm far away from the substrate. It is seen that the columnar sample (Figs. 4b and 5b) shows a strong <001> texture along the build direction, and the maximum texture intensity is approximately ~12 (see Fig. 4c). In contrast, the equiaxed sample (Figs. 4e and 5e) possesses an overall random texture. The <001> texture intensity is significantly reduced, with a maximum texture intensity of ~2 (see Fig. 4f). Our results demonstrate that by employing a specific current, the crystallographic texture and grain size can be engineered through the WAAM process.

The X-ray diffraction patterns for both produced samples are presented in Fig. 6. It should be noted that these measurements were performed in the *X-Z* plane of the samples (refer to Fig. 2). For both conditions, a single-phase Face Center Cubic (FCC) structure, typical of Inconel 625, is indexed. No precipitates were identified for columnar and equiaxed samples. Intermetallic phases such as γ″ Ni_3(Nb, Al, Ti), δ-Ni_3(Nb, Mo) or carbides, which can usually be found in casting and forging of Inconel 625 were not detected in the XRD patterns. If they exist, their volume fraction is below the resolution of conventional XRD laboratorial sources (3–5 vol%) [15]. Another interesting feature that is observed in the diffraction patterns is related to the texture. While for the columnar sample, the strongest and less intense peaks are the (220) and (111), respectively, for the equiaxed sample, this changes to (111) and (220). This also qualitatively evidences that the selected process parameters can modify the material texture.

The microstructure of the samples in different areas of the produced samples was further investigated by TEM, as detailed in Fig. 7. It is

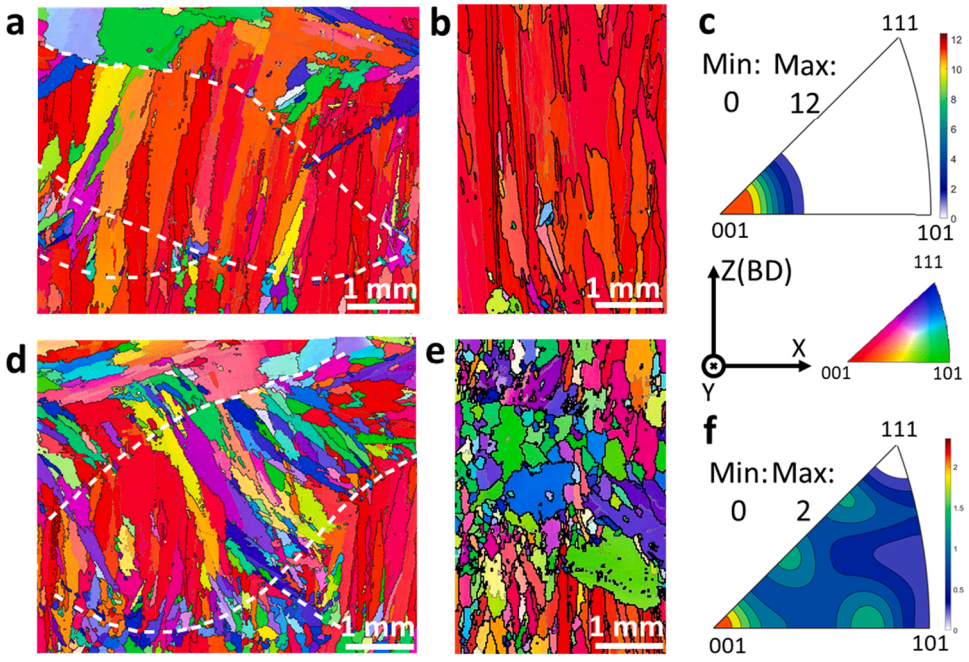

Fig. 4. EBSD orientation maps observed along the *Z*-axis from the *X-Z* plane melt pools at the top layer of the (a) columnar sample and (d) equiaxed sample, dashed line outlines the melt pool boundary. EBSD orientation maps observed from middle position of the *X-Z* plane of (b) columnar sample and (e) equiaxed sample, and inverse pole figures measured from the middle position of the *X-Z* plane of (c) columnar sample and (f) equiaxed sample.

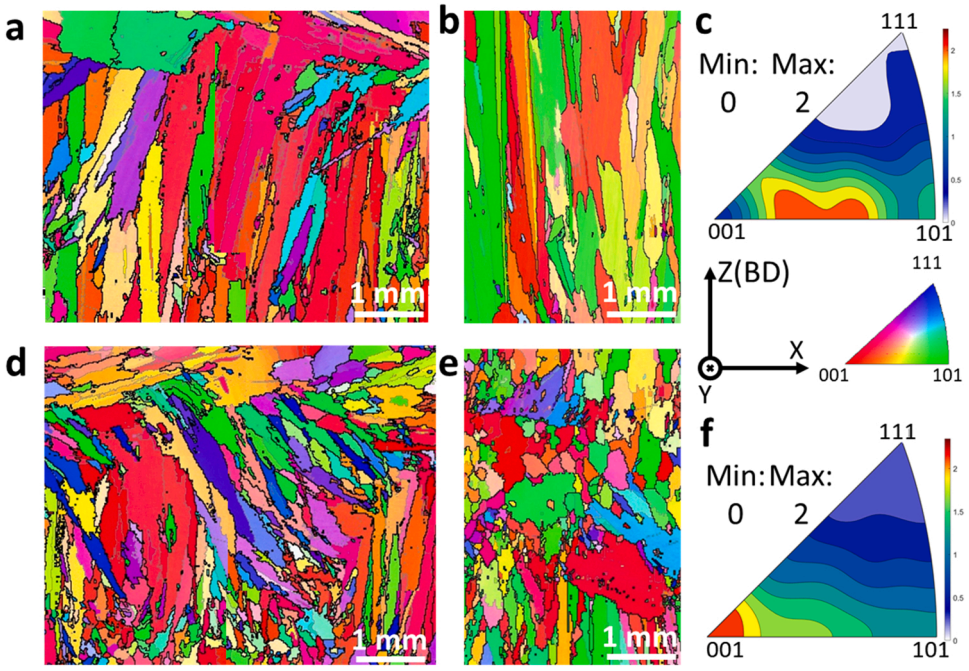

Fig. 5. EBSD orientation maps along the *X*-axis observed from the *X-Z* plane melt pools at the top layer of the (a) columnar sample and (d) equiaxed sample, EBSD orientation maps observed from middle position of the *X-Z* plane of (b) columnar sample and (e) equiaxed sample, and inverse pole figures measured from the middle position of the *X-Z* plane of (c) columnar sample and (f) equiaxed sample.

evident from the selected area diffraction patterns, that the matrix of the alloy is γ-Ni, and a larger number of dislocations exist in both the columnar and equiaxed samples (Fig. 7a-b). The dislocation density is determined from the EBSD data as detailed in Section 4.2.2.

Fig. 8 shows the local morphology of the WAAM Inconel 625 samples as obtained by SEM, and the results of the corresponding composition analysis. Some small particles are also observed in the SEM image on the surfaces of both the columnar (Fig. 8a) and equiaxed samples (Fig. 8h). The elemental distribution map shows the presence of globular Nb- and Ti-rich precipitates with an average size of about 1.3 μm in both samples (Fig. 8e–g, l–n). Fig. 9 shows the results of spot analysis by EDS of precipitated phases. The specific content is listed in Table 3. Combined the results of previous studies [41,42] with spot analyses indicated that these small particles are MC-type carbides with Nb and Ti enrichments. It is also noted that compared with the γ matrix (spot 1), some particles have extremely high Nb content (50 wt%) and low Ni content (20 wt%),

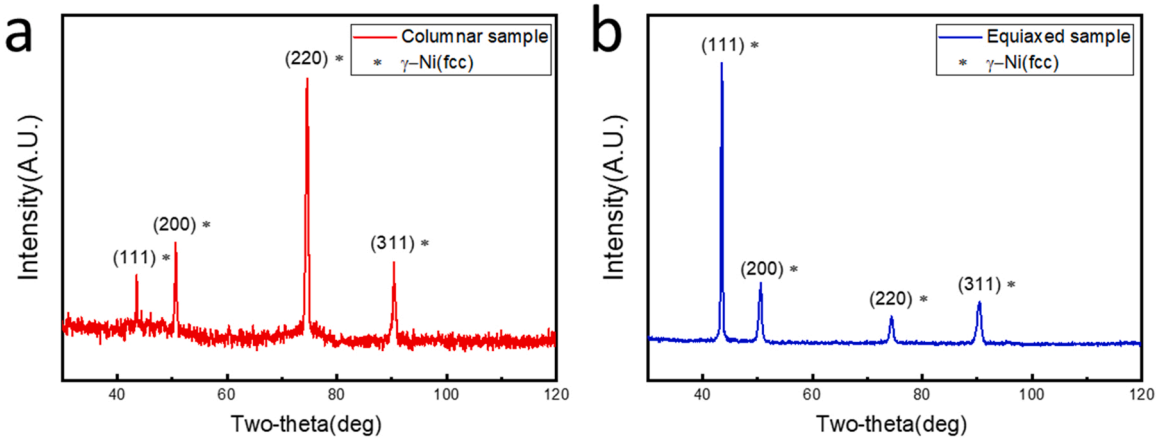

Fig. 6. XRD profiles for the *X-Z* plane of the deposited samples: (a) columnar sample; (b) equiaxed sample.

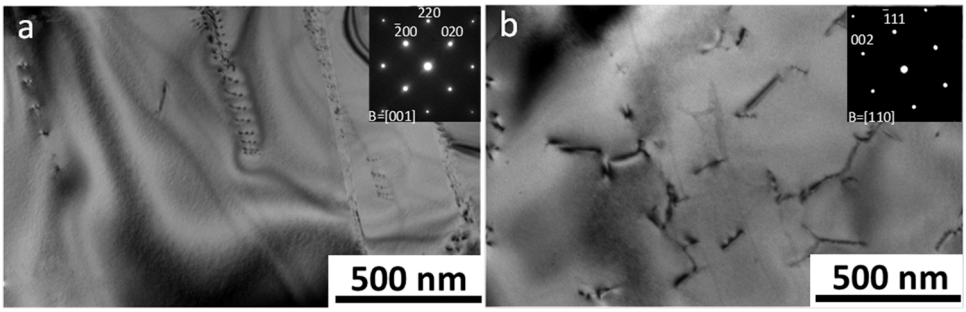

Fig. 7. Typical TEM images for different samples: (a) columnar sample; (b) equiaxed sample.

and its composition is near that of Nb-based MC-type carbides (such as spot 2). Some other MC carbides containing a lower amount of Nb (20 wt%), the higher content Ni (45 wt%), and a significant enrichment of Ti (5.0 wt%) (such as spot 3) were also observed. The volume fractions of these precipitates in columnar and equiaxed samples are determined to be about 0.74 % and 0.65 %, respectively. The low volume fraction of these precipitates justifies why these were not detected in the XRD patterns.

Figs. 10 and 11 depicts the morphology and the internal microstructure of the melt pools at the top layer of columnar and equiaxed samples, respectively. From the point of view of process parameters, while keeping the same traveling speed, the increase of current will result in an increased LED. As a consequence, the melt pool size will be deeper and larger. This is confirmed by the measurements of the melt pool size in Figs. 10a and 11a. Based on the pixel count, the melt pool depth (D) of columnar sample is determined to be roughly 4.2 $\pm$ 0.18 mm. This is indeed a smaller value than that of the equiaxed sample (5.5 $\pm$ 0.21 mm). The width (W) of the melt pool of columnar and equiaxed samples is 12.1 $\pm$ 1.4 and 14.4 $\pm$ 0.91 mm, respectively. A highly oriented epitaxial dendritic microstructure developed in the columnar sample (Fig. 10a). In opposition, misaligned cells grew perpendicularly to the melt pool border and towards the centre of the melt pool in the equiaxed sample (Fig. 11a). Figs. 10b-c and 11b-c show magnified images of the dendrites (columnar and equiaxed samples, respectively). The Secondary Dendrite Arm Spacing (*SDAS*) of the two samples was measured from the optical micrographs. The *SDAS* of columnar and equiaxed samples was measured to be of 9.5 $\pm$ 1.8 and 17.6 $\pm$ 2.0 μm, respectively. The morphology of the melt pool is an important factor that may influence the grain structure [43]. The distinct grain morphologies arise from the thermal gradient (G_L) and solidification velocity (R_L) conditions experienced by the material [22, 23,44]. To quantify G_L and R_L, the dimensions of the melt pool, viz. length (L) and width (W), should be estimated. In this research, we adopted a theoretical model to compute the temperature field in the neighborhood of the heat source in the WAAM process for both columnar and equiaxed samples. With the width (W) available from measurements, the length can be backcalculated from the L/W rate of the melt pool determined using the temperature distribution plot given by the theoretical model. Details of this approach and its symbolical and graphical presentation can be found in Section 4.1.

3.2. Mechanical properties

Fig. 12a depicts a set of typical true stress-strain tensile curves along the build direction (Z-axis) for the two Inconel 625 alloy samples obtained at room temperature. Overall, both samples exhibit superior mechanical properties, showing both high ultimate tensile strength (~1000 MPa) and large uniform elongation (~40 %). Specifically, by comparing the true stress–strain curves of the equiaxed and columnar samples, it can be seen that the yield strength of the former is superior to the latter (404 $\pm$ 14 MPa vs. 310 $\pm$ 5 MPa, respectively). On the other hand, the uniform elongation of the equiaxed samples is slightly lower. Note that the two samples have similarities in the flow stress-strain relationship. For a true strain between ~0.05 and ~0.25, the stress–-strain curve assumes a slightly concave shape. This indicates that, at this strain level, a secondary strain hardening seems to occur. This is more clearly seen in Fig. 12b, where the variation of the work hardening rate vs. true strain is plotted for both the columnar and equiaxed samples. It is seen that both the columnar and equiaxed samples show very similar trends regarding their work hardening response, revealing three stages of work hardening typical of alloys with low Stacking Fault Energies (SFEs) [45]. Both curves show an initially continuous decrease in their work hardening rate (stage A), which is similar to the 3rd hardening stage of alloys with high SFE [46]. After reaching a minimum hardening

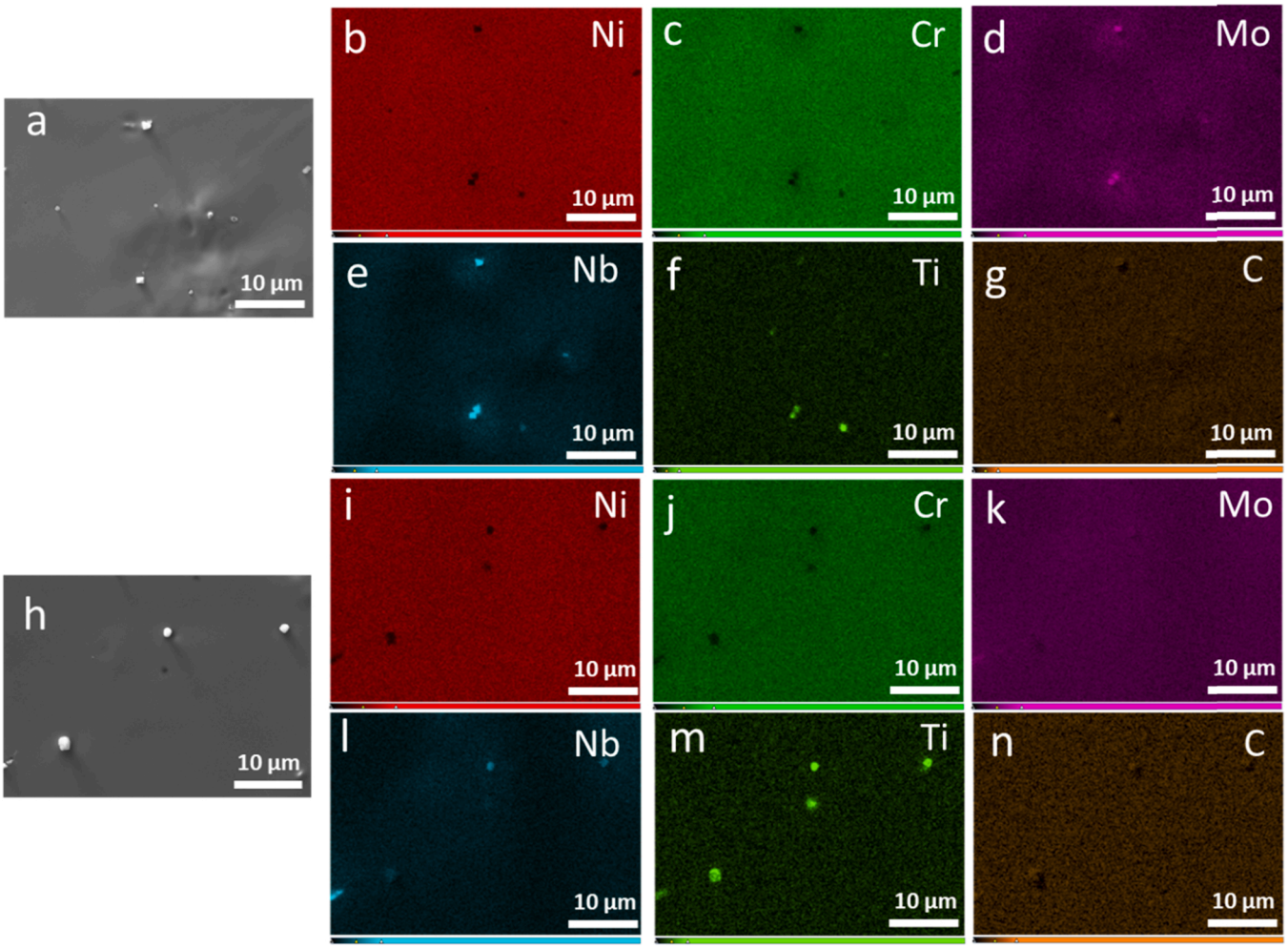

Fig. 8. Compositional surface analysis of the WAAM - processed Inconel 625. Local SEM morphology and elemental distribution maps of the produced samples: (a–g) columnar sample; (h–n) equiaxed sample.

rate at a true strain between 0.05 and 0.1, the hardening rate starts to rise (stage B). At the end of the stage B, the work hardening rate can increase up to a hardening coefficient of about $G/40$ (G is the shear modulus). This is consistent with previous studies on low SFE alloys, such as TWIP steel ($G/30$) [47]. As the flow stress further increases, the strain hardening rate starts to decrease rapidly until failure (stage C).

4. Discussion

4.1. Implications of thermal parameters on the grain structure

Different melt pool shapes might aid in modifying the crystallographic texture and grain structure in the fabricated parts. Sun et al. [48] reported that within a larger melt pool, a $< 011 >$ crystallographic texture along build direction is favored, while for a flatter melt pool, a common $<001>$ crystallographic texture along build direction is usually developed. The grain morphology evolution is determined by the local solidification conditions, including the thermal gradient (G_L) and growth rate (R_L) at the liquid/solid interface of the melt pool [49]. When the values of G_L and R_L satisfy the condition for CET, equiaxed grains will form in the melt pool [22,23,44]. The volume fraction of equiaxed grains in the solidified melt pool can be changed by varying the process parameters as exemplified elsewhere [22,50].

The existence of CET in the WAAM-fabricated Inconel 625 alloy suggests that manipulating the process parameters may break up the solidification conditions favouring the epitaxial growth along the build direction. Based on the following models, it is possible to roughly calculate the thermal gradient (G_L) and solidification rate (R_L) of both produced samples (columnar and equiaxed) during solidification. As $G_L = C_L/R_L$, where C_L is the local cooling rate, a prerequisite for quantifying G_L and R_L is the estimation of C_L in the melt pool for the present 625 alloy using Eq. (2), which requires a simplification of the Inconel 625 alloy into a binary alloy. In the nickel-based alloy, the partition coefficients of Mo, Cr and most other elements are close to 1 [44] which means that the solid-liquid solute content is kept constant, while the partition coefficient of Nb is about 0.2–0.5, which indicates that the solid-liquid concentration difference during solidification is relatively large, that is, the effect of Nb on dendrite growth is more critical [44,51]. Therefore, we finally simplified the alloy into a Ni-3.6Nb binary system according to the concentration of Nb in the material. The thermodynamic parameters are shown in Table 4 [44,51]. The local cooling rate (C_L) can be estimated by bringing the measured *SDAS* into the following model [52]:

$$SDAS = 5.5\left(-\frac{\Gamma D_l \ln\left(\frac{C_{eut}}{C_0}\right)}{m_l(1-k_0)(C_{eut}-C_0)}\right)^{\frac{1}{3}}\left(\frac{\Delta T_0}{C_L}\right)^{\frac{1}{3}} \quad (2)$$

where D_l is the diffusion coefficient of Nb in the liquid metal, Γ is the Gibbs-Thomson coefficient, C_0 is the concentration of Nb in the fluid, C_{eut} is the concentration in the liquid at the eutectic point, $_{ml}$ is the liquidus slope, k_0 is the binary equilibrium partition coefficient and ΔT_0 is

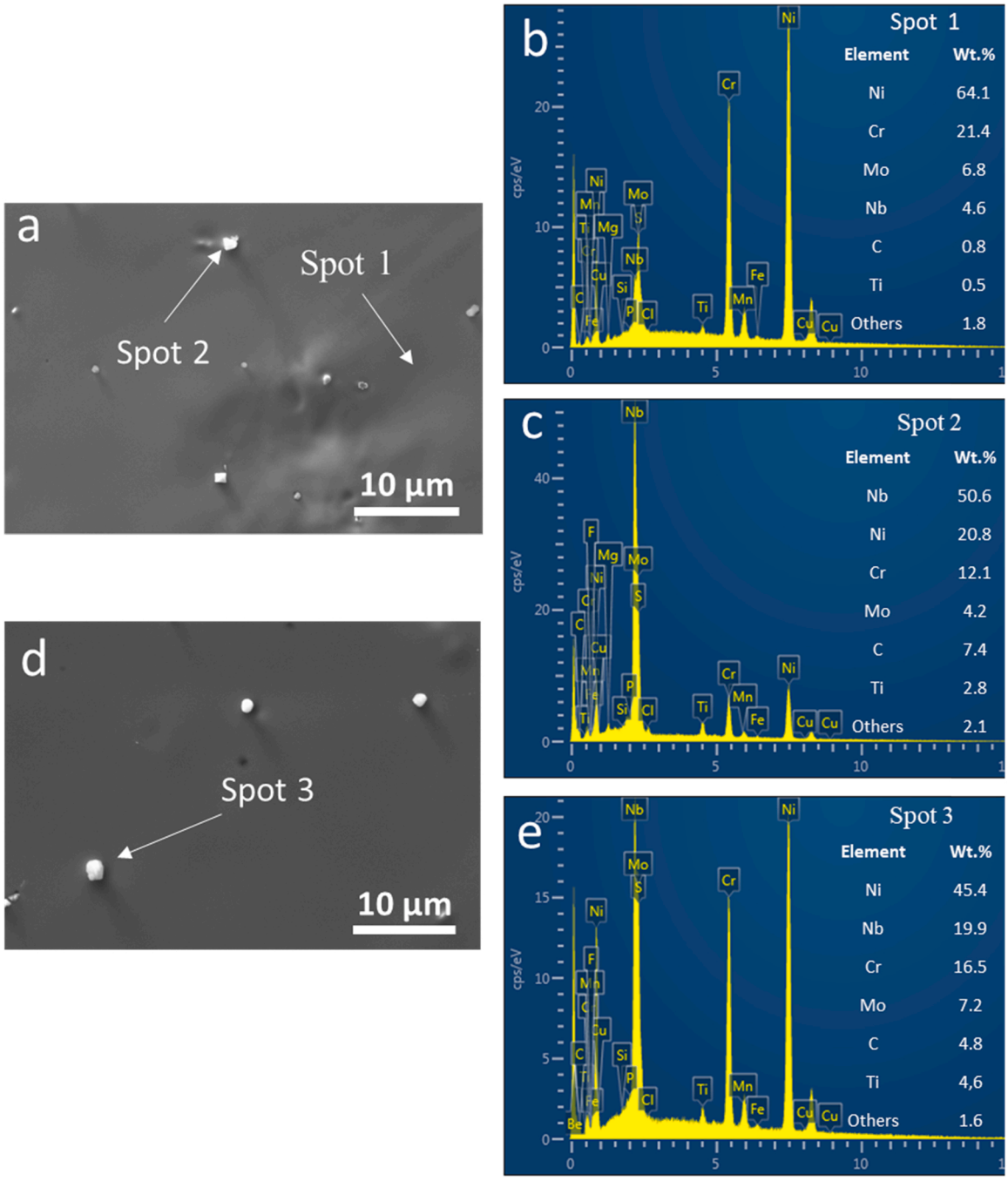

Fig. 9. SEM imaging of (a) columnar sample and (d) equiaxed sample. A typical EDS spectrum showing the presence of (b) Spot 1, (c) Spot 2 and (e) Spot 3.

Table 3
Chemical composition of precipitates at different positions (wt%).

	Ni	Cr	Nb	Mo	C	Ti	Others
Spot 1	64.1	21.4	4.6	6.8	0.8	0.5	1.8
Spot 2	20.8	12.1	50.6	4.2	7.4	2.8	2.1
Spot 3	45.4	16.5	19.9	7.2	4.8	4.6	1.6

the non-equilibrium solidification range. The local cooling rate, C_L, was estimated by Eq. (2), yielding 5.21×10^2 and 0.82×10^2 K/s for the columnar and equiaxed samples, respectively, as listed in Table 5.

An indispensable step in the quantification of G_L and R_L for the discussion of their impact on the morphology of grain shape is the estimation of the length (L) and width (W) of the melt pool, as schematically illustrated in Fig. 13a. It should be clarified that the time required to solidify from B to C with the distance of the melt pool depth (D) is equal to the time required from A to C with the distance of the melt pool length (L). If the internal solidification rate is assumed to be constant, R_L can be determined by $R_L = DV_t/L$ [52]. With the width of melt pool (W) already available from data reported in Section 3.1, it is necessary to estimate the value of L. To this end, we adopted the classical theoretical solution of the temperature field in the vicinity of a heat source in the welding process by Rosenthal et al., which is expressed by Eq. (3) [48]:

$$T = T_0 + \frac{P}{2\pi Kr}\exp\left(-\frac{V_t(x+r)}{2\alpha}\right) \tag{3}$$

where T_0 is the average interlayer temperatures of the top deposited layer, P is the power, K is the thermal conductivity, r is the radial

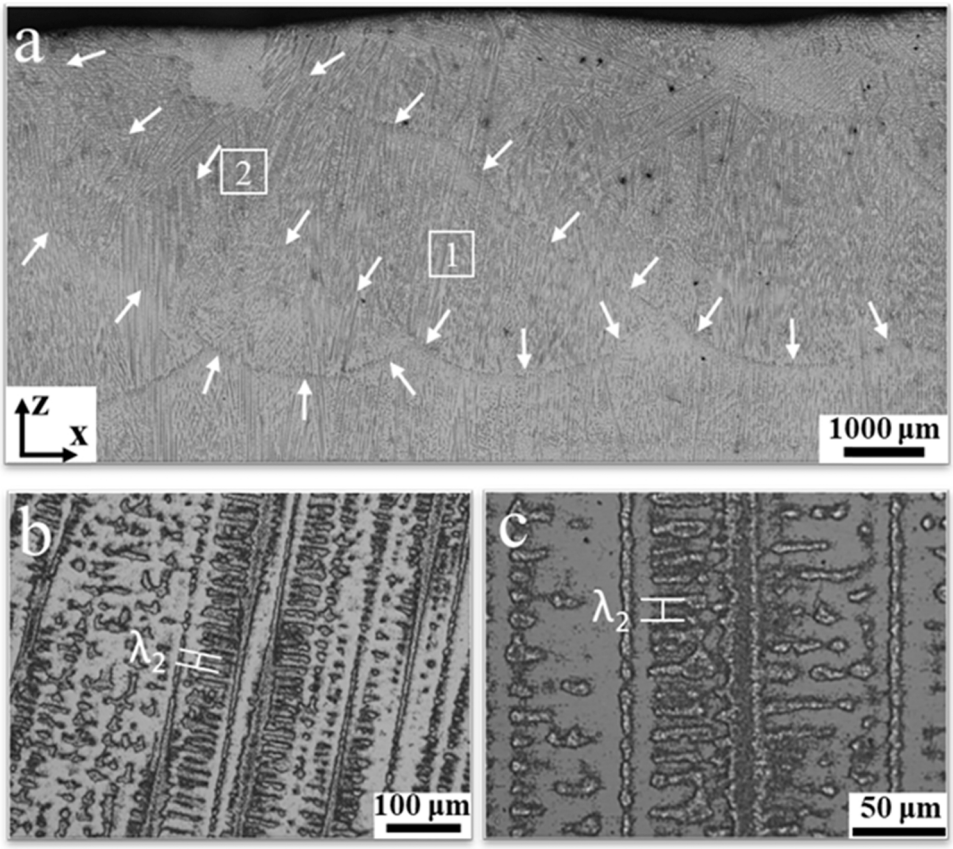

Fig. 10. Microstructure of the columnar sample at the top layer, (a) OM image showing the dendritic microstructure and the melt pool boundary, (b) magnified image of region 1, (c) magnified image of region 2.

distance from the moving point, α is the thermal diffusivity. Fig. 13b shows the variation of the interlayer temperature experimentally measured by the infrared thermometer with the deposited layers. For the columnar sample processed with 125 J/mm, the average temperature of each layer increased linearly with the number of layers in the first 10 layers (from 379 K to 811 K), and there was almost no significant change in the temperature of each layer after 10th layer is deposited, with the average temperature being of ≈ 818 K. Similarly, for the first 10 layers of the sample obtained with 140 J/mm, the average temperature of each layer increased linearly with the number of layers (from 443 K to 819 K), and there was no appreciable change in the temperature afterwards with the average temperature recorded being of ≈ 849 K (Fig. 13b). Both samples show the same trend, i.e., interlayer temperatures remain roughly constant after 10 layers are deposited. As the specimens for microstructural and mechanical characterization were extracted at layers well above the first 10 deposited ones, we averaged the interlayer temperatures in the plateau region in Fig. 13b as T_0 for Eq. (3). Correspondingly, T_0 takes 818 and 849 K for the columnar and equiaxed samples, respectively. We then utilized MATLAB to simulate and plot the temperature distribution for the two samples. Fig. 13c-d depicts the Rosenthal's solutions for the columnar and equiaxed samples, respectively, from which the L/W ratio of length L and width W of the melt pool can be estimated. The length of the melt pool (L) is backcalculated as the product between the L/W ratio of the melt pool measured from the temperature distribution plot and W. Correspondingly, the R_L value can be estimated by $R_L = DV_t/L$. Finally, the local temperature gradient can be obtained through equation $G_L = C_L/R_L$, listed in Table 5.

Fig. 14 shows the G_L vs. R_L plot on a reference solidification map of Inconel 625. The calculated G_L and R_L for the columnar and equiaxed samples are plotted in the Inconel 625 alloy solidification map, as depicted in Fig. 14. It can be seen that the increase in the electric current mainly affects the G_L value for the Inconel 625 WAAM-fabricated parts. More specifically, the G_L value is reduced from 2.65×10^5 to 4.10×10^4 K/m, i.e., one order of magnitude, which enables for the solidification conditions in the melt pool to favor the formation of equiaxed grains. The solidification map detailed in Fig. 14 details that the calculated (R_L, G_L) values for both columnar and equiaxed samples explained the phenomenon of CET observed in both samples. The corresponding (R_L, G_L) range of values for the work of Hu [44] are also included for comparison (see the area outlined by the white square in Fig. 14). From the above analysis, it can be concluded that increasing the current will cause the LED to increase, resulting in a larger melt pool, slower cooling rate and lower thermal gradient at comparable solidification velocities (hence smaller G_L/R_L ratio). This means that it may offer a thermal environment satisfying the required solidification conditions for the nucleation of equiaxed grains.

4.2. Relationship between microstructures and the mechanical properties

In order to have a better understanding on why the yield strength of the equiaxed sample is higher than that of the columnar sample, the contribution of each strengthening mechanism is calculated. There are four main strengthening mechanisms in metallic alloys: solid-solution strengthening, strain strengthening (dislocation strengthening), precipitation strengthening and refinement strengthening (grain boundary strengthening).

4.2.1. Precipitation strengthening

The strengthening contribution ($\Delta\sigma_p$) result from the precipitates can be estimated based on the Orowan mechanism [54]:

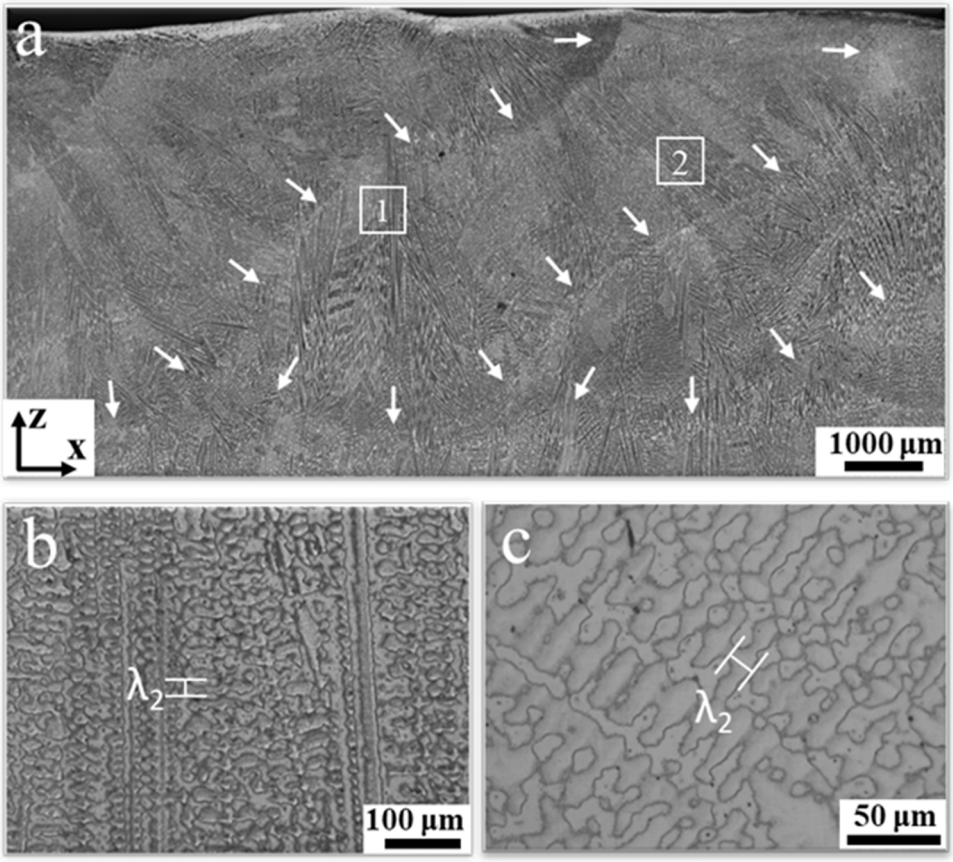

Fig. 11. Microstructure of the equiaxed sample at the top layer, (a) OM image showing the dendritic microstructure and the melt pool boundary, (b) magnified image of region 1, (c) magnified image of region 2.

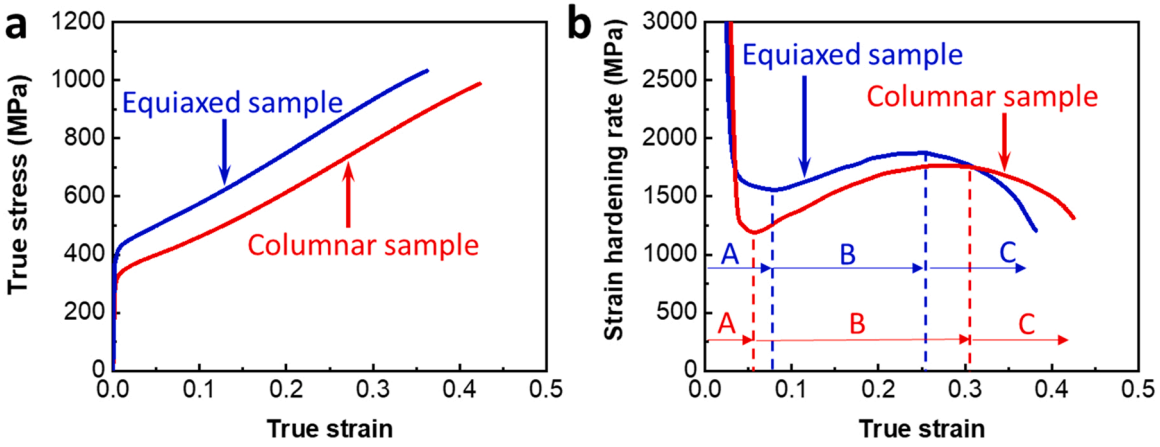

Fig. 12. (a) True stress-strain tensile curves of WAAM-fabricated Inconel 625 samples along the build direction (*Z*-axis); (b) Work hardening behaviour of the columnar and the equiaxed samples.

Table 4
The thermophysical properties of Inconel 625 alloy.

Γ[53] (Km)	D_l[53] (m^2/s)	C_0 (at %)	C_{eut} (at %)	$_{ml}$ (K/at %)	k_0	ΔT_0 (K)	K[53] (W/ (m K))	α[53] (m^2/s)
3.65×10^{-7}	3×10^{-9}	2.33	16	-10.5	0.48	95	30.1	5.5×10^{-6}

$$\Delta\sigma_p = \frac{0.4MGbln\left(\frac{2\bar{r}}{b}\right)}{\pi\sqrt{1-v}2\bar{r}\left(\sqrt{\frac{\pi}{4f}}-1\right)} \quad (4)$$

where $M = 3.06$ is the mean orientation factor for the fcc polycrystalline matrix [34]; G is the shear modulus, 81.4 GPa; $v = 0.28$ is Poisson's ratio of the Inconel 625 matrix; b is the magnitude of the Burgers vector,

Table 5
The measured *SDAS* and the calculated solidification conditions.

Sample	V_t (mm/s)	*SDAS* (μm)	G_L (K/s)	*L/W*	R_L (m/s)	G_L (K/m)
Columnar sample	10	9.5	5.21×10^2	1.76	1.97×10^{-3}	2.65×10^5
Equiaxed sample	10	17.6	0.82×10^2	1.91	2.00×10^{-3}	4.10×10^4

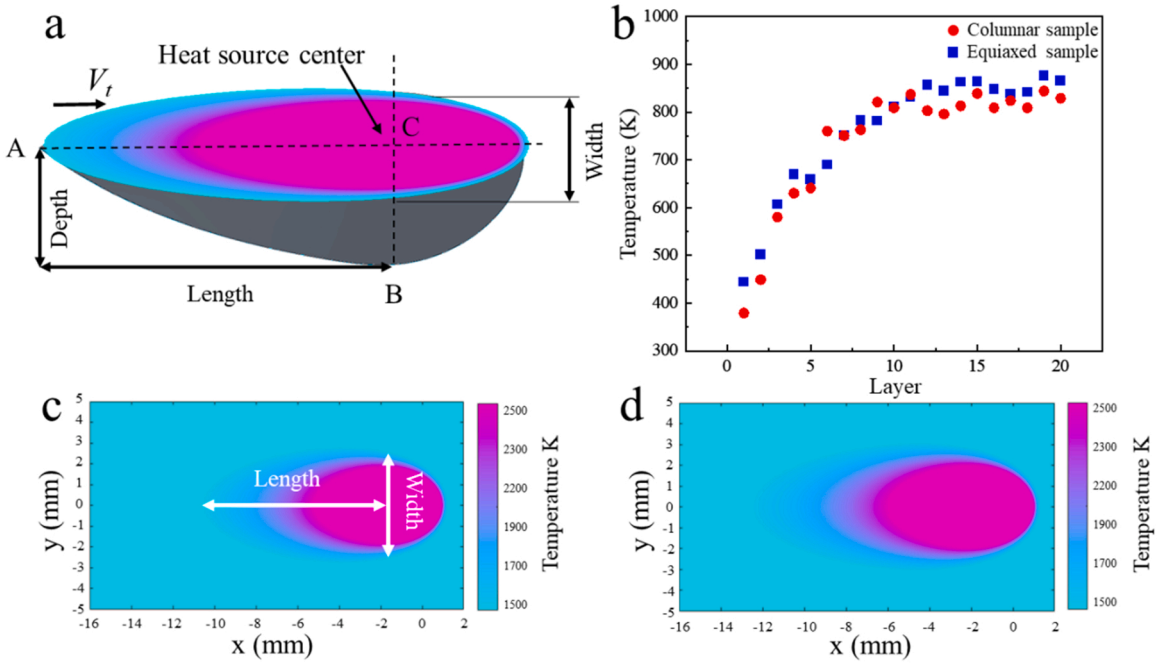

Fig. 13. (a) Schematic diagram of typical melt pool shape model during WAAM. (b) Trend of average temperature after completion of each deposited layer. (c) and (d) are melt pool morphology simulations on the plane surface for columnar and equiaxed samples, respectively, using the Rosenthal's solution.

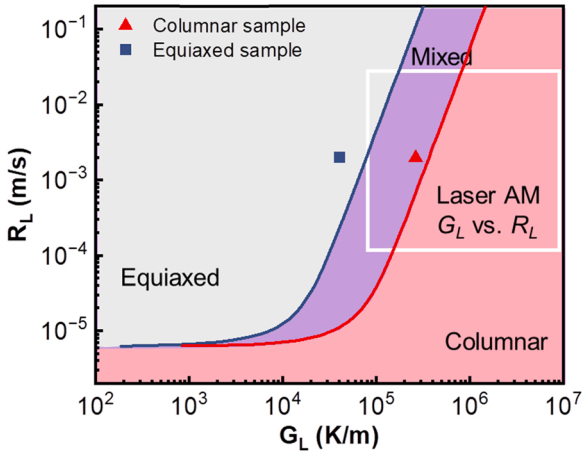

Fig. 14. Plot of G_L vs. R_L for the columnar and equiaxed samples in the Inconel 625 solidification map (based on the original map of Hu [44]). The area outlined by the white square indicates (G_L, R_L) values for laser solid forming Inconel 625 samples obtained from Ref. [24].

0.25 nm. $\bar{r} = \sqrt{2/3}\, r$ is the mean radius of a circular cross section in a random plane for a spherical precipitate, r is the average radius of precipitates, 1300 nm. f is the volume fraction of precipitates, i.e., 0.74 % and 0.65 % for columnar and equiaxed samples, respectively. Consequently, the strengthening contributions from the precipitates $\Delta\sigma_p$ for the columnar and equiaxed samples are calculated to be 4.29 MPa and 3.99 MPa, respectively. The strengthening contribution from the precipitates is extremely small, hence the contribution of precipitation strengthening to yield strength can be ignored in this case.

4.2.2. *Grain size effect*

Grain boundaries have been well considered as strong obstacles for dislocation motion, and the contribution to the yield strength caused by grain boundaries is empirically determined by the Hall-Petch equation [55]:

$$\sigma_y = \sigma_0 + kd^{-0.5} \tag{5}$$

where σ_0 is a friction stress, k is the Hall-Petch coefficient (~750 MPa $\mu m^{1/2}$ for Inconel 625) [56]. The strength enhancement induced by grain boundary strengthening in the present WAAM samples can be written as $\Delta\sigma_s = kd^{-0.5}$. Using the average grain sizes as determined by the EBSD data in Section 3.1, the contributions of grain boundary strengthening in the columnar and equiaxed sample are calculated to be 41.7 MPa and 50.3 MPa, respectively. These results show that the effect of grain size variation on the yield strength can be almost neglected.

4.2.3. *Dislocation strengthening*

Generally, the introduction of dislocations by plastic deformation results in the decrease of the average distance between dislocations and consequently dislocations start blocking the motion of each other. As the resistance to dislocation motion rises with the dislocation density, the material strength increases [57]. During WAAM of the Inconel 625 alloy, residual thermal stresses develop and these promote the generation of dislocations in the produced parts. This happens due to the non-equilibrium, rapid and repeated heating and cooling [58]. Therefore, the dislocations associated to the processing conditions can also contribute to an increase in the material yield strength, as described by

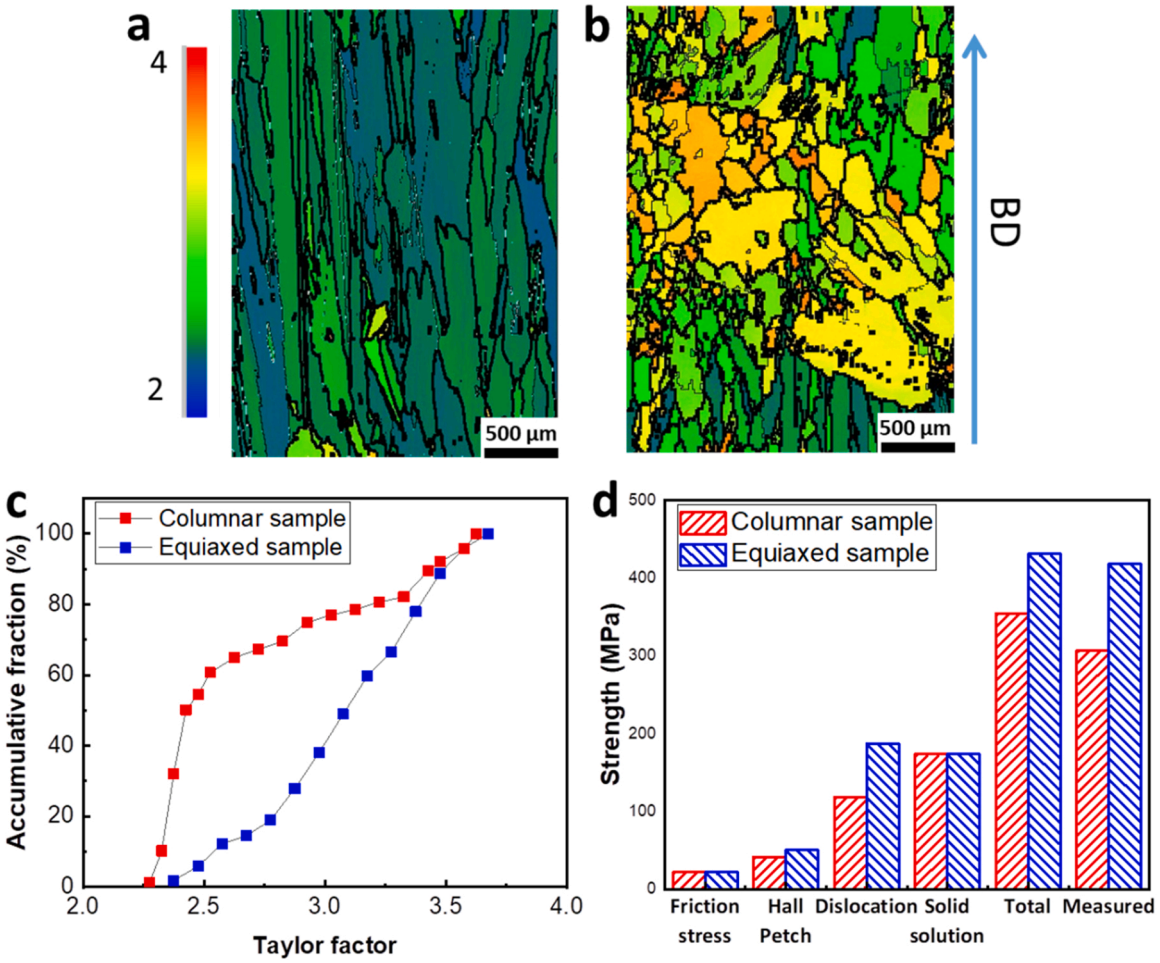

Fig. 15. Taylor factor maps along the tensile direction (BD) for (a) columnar sample and (b) equiaxed sample. (c) Accumulative fraction of Taylor factors for the columnar and equiaxed samples. (d) Contribution of different strengthening mechanisms for the yield strength of the two samples. The measured yield strengths are also included for comparison.

the Taylor equation [59]:

$$\Delta\sigma_\rho = M\alpha Gb\sqrt{\rho} \tag{6}$$

Where G is the shear modulus (80 GPa), b is the Burgers vector (0.25 nm) [60], α is a constant (0.6), ρ is the dislocation density, and M is the Taylor factor. In the present study, the dislocation density was determined by the analysis of the Kernel Average Misorientation (KAM), which was obtained directly from the EBSD data. The defect density inside the grains is calculated as $\rho = 2\theta_{KAM}/xb$, where θ_{KAM} is kernel average misorientation, x is the unit length and b is the magnitude of the Burgers vector. X is defined as x = ns, where n is the second neighbour and s is the step size. Correspondingly, the dislocation density (ρ) of the columnar and equiaxed samples is roughly estimated to be 2.06×10^{13} m^{-2} and 2.38×10^{13} m^{-2}, respectively, suggesting that the changes in the process parameters do not drastically modify the dislocation density. As proposed by Taylor [61], if each grain in a polycrystalline material is assumed to undergo the same plastic deformation, the active combination of slip systems with minimum energy could be obtained based on the orientation of the grain relative to the deformation reference frame. The Taylor factor (M), as a sum of the glide shears, then serves as a measure of the yield strength of a grain due to its specific orientation. A large Taylor factor means that a high stress is required to initiate the dislocation slip to accommodate the plastic deformation of the grain [62]. Fig. 15a-b displays examples of the Taylor factor maps for the grains with tensile direction parallel to the build direction in the columnar and equiaxed samples, respectively. A distinct difference on the Taylor factors of columnar and equiaxed grains is observed, which is more clearly revealed by plotting the accumulative fraction of the Taylor factors in the columnar and equiaxed samples (Fig. 15c). The distribution of the Taylor factors of the equiaxed sample apparently shifts to larger values compared to the columnar one. On average, the Taylor factor of the equiaxed sample (3.15) is 32 % larger than that of the columnar sample (2.39), suggesting that more energy is required to deform the equiaxed grains, i.e., the yield strength rises. This is further verified by the quantitative calculation using the Taylor Eq. (5) with the obtained dislocation density and average Taylor factor. The strength enhancement induced by dislocation strengthening of the equiaxed sample is 187.3 MPa, which is obviously higher than that of the columnar sample, calculated to be 118.6 MPa. As the dislocation density is similar for both samples, the significant dislocation strengthening of the equiaxed sample can be ascribed to the larger Taylor factor.

4.2.4. Solid-solution strengthening

Roth et al. [63] proposed that the solid solution strengthening arising from various solute atoms in a multicomponent alloy could be considered as the superposition in the strengthening of individual solutes, which individually have different potencies. The equation is written as:

$$\Delta\sigma_C = \sum_i \left(\frac{d\sigma}{\sqrt{dC_i}}\sqrt{C_i}\right) \tag{7}$$

where C_i is the concentration of solute i and $\frac{d\sigma}{\sqrt{dC_i}}$ is the strengthening

Table 6
Content of solution elements for different samples and solid-solution strengthening constants for elements addition ($d\sigma/dc_i^{0.5}$) [44].

	Ni	Cr	Mo	Nb	Fe	Si
Columnar sample	0.662	0.25	0.058	0.0234	0.0027	0.0022
Equiaxed sample	0.654	0.255	0.057	0.0234	0.0037	0.0047
Constants for each element	–	337	1015	1183	153	275

coefficient of solute *i*. The results of chemical composition analysis in the two samples and the solid solution strengthening coefficients for the addition of elements are shown in Table 6. By using the Eq. (7) to estimate the solid solution strengthening, the solid solution strengthening values of the columnar and equiaxed samples are 173.5 MPa and 173.6 MPa, respectively.

Overall, the contributions of different strengthening mechanisms can be added linearly [64]. Therefore, the yield strength (σ_y) of the WAAM-processed Inconel 625 alloy can be described as:

$$\sigma_y = \sigma_0 + \Delta\sigma_s + \Delta\sigma_\rho + \Delta\sigma_C \quad (8)$$

where σ_0 is ~21.8 MPa [65]. The strengthening increments caused by grain boundaries, dislocations, and solute atoms are shown in Fig. 15d. Note that the calculated total yield strength of the two samples is 430 MPa and 355 MPa, respectively. They are in a good agreement with the previously measured yield strengths for each sample. Moreover, the difference (68.7 MPa) on the dislocation strengthening between two samples is within the same order of magnitude of that between the measured yield strength (111 MPa). Therefore, the higher yield strength of the equiaxed sample when compared to the columnar sample may be attributed to its larger dislocation strengthening, arising from the large average Taylor factor based on the Taylor equation.

5. Conclusions

Through the exploration of both the microstructure and the mechanical properties in WAAM fabricated Inconel 625, the following conclusions can be drawn:

(1) The electric current exerts a significant effect on the grain morphology and orientation. Under the same traveling speed, increasing the current is effective in eliminating the columnar grains with crystal direction <001> parallel to the build direction. Instead, the grains become more equiaxed and a near random crystallographic texture is obtained.
(2) The approximate solidification conditions (G_L, R_L, C_L) during WAAM of Inconel 625 alloy were determined and coupled with existing criteria for CET during solidification of Inconel 625 alloy. It was confirmed that the CET during WAAM could be promoted by tweaking the process parameters so that the thermal cycle conditions would be modified. The G_L value at the solid-liquid interface in the melt pool decreases by roughly one order of magnitude in the sample fabricated with large current, which allows for the nucleation and growth of equiaxed grains.
(3) With the occurrence of CET in the WAAM-fabricated 625 alloy sample, the equiaxed sample exhibits a greater yield strength (increase of 36 %) compared to the columnar sample. A quantitative analysis on the various strengthening mechanisms indicates that grain boundary and solid-solution strengthening contribute to the yield strength similarly in both samples. However, the larger average Taylor factor of the equiaxed sample offers an enhanced dislocation strengthening as compared to the columnar sample, accounting for roughly the same enhancement on the measured yield strength.

CRediT authorship contribution statement

J.P. Oliveira: Writing – review & editing, Funding acquisition, Investigation. **Y. Zhang:** Writing – review & editing, Resources, Project administration, Funding acquisition. **S. Li:** Writing – original draft, Investigation. **Y.H. Zhao:** Resources. **Y. Cheng:** Resources. **Y. Li:** Methodology. **K.H. Wang:** Resources. **Z.W. Jiang:** Methodology. **H.X. Chen:** Methodology. **Y. Zou:** Resources. **S. Tang:** Methodology. **J.Z. Leng:** Methodology. **J.Y.Li:** Resources, Methodology.

Declaration of Competing Interest

The authors declare that they have no known competing financial interests or personal relationships that could have appeared to influence the work reported in this paper.

Acknowledgements

This work was supported by the National Natural Science Foundation of China (grants 51 601 091 and 51 971 112), the Natural Science Foundation of Jiangsu Province (grants BK 20 160 826 and BK 20 200 503), the Six Talent Peaks Project of Jiangsu Province (grant 2017-XCL-051), the Fundamental Research Funds for the Central Universities (grants 30 917 011 106 and 30 919 011 405), and Key Research and Development Plan of Jiangsu Province (BE 2 020 085). JPO acknowledges Fundação para a Ciência e a Tecnologia (FCT - MCTES) for its financial support via the project UID/667/2020 (UNIDEMI). JPO also acknowledges the funding of CENIMAT/i3N by national funds through the FCT - Fundação para a Ciência e a Tecnologia, I.P., within the scope of Multiannual Financing of R&D Units, reference UIDB/50 025/2020–2023.

References

[1] A. Paolini, S. Kollmannsberger, E. Rank, Additive manufacturing in construction: a review on processes, applications, and digital planning methods, Addit. Manuf. 30 (2019), https://doi.org/10.1016/j.addma.2019.100894.
[2] E. Macdonald, R. Wicker, Multiprocess 3D printing for increasing component functionality, Science 353 (2016), https://doi.org/10.1126/science.aaf2093.
[3] X.F. Sun, W. Song, J.J. Liang, J.G. Li, Y.Z. Zhou, Research and development in materials and processes of superalloy fabricated by laser additive manufacturing, Acta Met. Sin. 57 (2021) 1471–1483, https://doi.org/10.11900/0412.1961.2021.00371.
[4] X.H. Chen, J. Li, X. Cheng, H.M. Wang, Z. Huang, Effect of heat treatment on microstructure, mechanical and corrosion properties of austenitic stainless steel 316L using arc additive manufacturing, Mater. Sci. Eng. A 715 (2018) 307–314, https://doi.org/10.1016/j.msea.2017.10.002.
[5] S.P. Narra, Powder bed fusion – metals, in: F.G. Caballero (Ed.), Encyclopedia of Materials: Metals and Alloys, Elsevier, Oxford, 2022, pp. 85–94, https://doi.org/10.1016/B978-0-12-819726-4.00107-1.
[6] R.M. Kindermann, M.J. Roy, R. Morana, P.B. Prangnell, Process response of Inconel 718 to wire + arc additive manufacturing with cold metal transfer, Mater. Des. 195 (2020), 109031, https://doi.org/10.1016/j.matdes.2020.109031.
[7] H. Yeung, B. Lane, J. Fox, Part geometry and conduction-based laser power control for powder bed fusion additive manufacturing, Addit. Manuf. 30 (2019), https://doi.org/10.1016/j.addma.2019.100844.
[8] B. Attard, S. Cruchley, C. Beetz, M. Megahed, Y.L. Chiu, M.M. Attallah, Microstructural control during laser powder fusion to create graded microstructure Ni-superalloy components, Addit. Manuf. 36 (2020), https://doi.org/10.1016/j.addma.2020.101432.
[9] Y.L. Hu, X. Lin, Y.L. Li, S.Y. Zhang, X.H. Gao, F.G. Liu, X. Li, W.D. Huang, Plastic deformation behavior and dynamic recrystallization of Inconel 625 superalloy fabricated by directed energy deposition, Mater. Des. 186 (2020) 108359–108375, https://doi.org/10.1016/j.matdes.2019.108359.
[10] C. Pleass, S. Jothi, Influence of powder characteristics and additive manufacturing process parameters on the microstructure and mechanical behaviour of Inconel 625 fabricated by Selective Laser Melting, Addit. Manuf. 24 (2018) 419–431, https://doi.org/10.1016/j.addma.2018.09.023.
[11] Y. Wang, R. Chen, X. Cheng, Y. Zhu, J. Zhang, H.M. Wang, Effects of microstructure on fatigue crack propagation behavior in a bi-modal TC11 titanium alloy fabricated via laser additive manufacturing, J. Mater. Sci. Technol. 35 (2019) 403–408, https://doi.org/10.1016/j.jmst.2018.10.031.
[12] J. Nguejio, F. Szmytka, S. Hallais, A. Tanguy, S. Nardone, M. Godino Martinez, Comparison of microstructure features and mechanical properties for additive manufactured and wrought nickel alloys 625, Mater. Sci. Eng. A 764 (2019), 138214, https://doi.org/10.1016/j.msea.2019.138214.

[13] A. Hadadzadeh, B.S. Amirkhiz, J. Li, M. Mohammadi, Columnar to equiaxed transition during direct metal laser sintering of AlSi10Mg alloy: effect of building direction, Addit. Manuf. 23 (2018) 121–131, https://doi.org/10.1016/j.addma.2018.08.001.
[14] C. Li, R. White, X.Y. Fang, M. Weaver, Y.B. Guo, Microstructure evolution characteristics of Inconel 625 alloy from selective laser melting to heat treatment, Mater. Sci. Eng. A 705 (2017) 20–31, https://doi.org/10.1016/j.msea.2017.08.058.
[15] S. Li, Q. Wei, Y. Shi, Z. Zhu, D. Zhang, Microstructure characteristics of Inconel 625 superalloy manufactured by selective laser melting, J. Mater. Sci. Technol. 31 (2015) 946–952, https://doi.org/10.1016/j.jmst.2014.09.020.
[16] H.Y. Wan, Z.J. Zhou, C.P. Li, G.F. Chen, G.P. Zhang, Effect of scanning strategy on grain structure and crystallographic texture of Inconel 718 processed by selective laser melting, J. Mater. Sci. Technol. 34 (2018) 1799–1804, https://doi.org/10.1016/j.jmst.2018.02.002.
[17] N. Raghavan, B.C. Stump, P. Fernandez-Zelaia, M.M. Kirka, S. Simunovic, Influence of geometry on columnar to equiaxed transition during electron beam powder bed fusion of IN718, Addit. Manuf. (2021), https://doi.org/10.1016/j.addma.2021.102209.
[18] T.M. Pollock, S. Tin, Nickel-based superalloys for advanced turbine engines: chemistry, microstructure and properties, J. Propul. Power 22 (2006) 361–374, https://doi.org/10.2514/1.18239.
[19] M.M. Kirka, Y. Lee, D.A. Greeley, A. Okello, M.J. Goin, M.T. Pearce, R.R. Dehoff, Strategy for texture management in metals additive manufacturing, Miner. Met. Mater. Soc. 69 (2017) 523–531, https://doi.org/10.1007/s11837-017-2264-3.
[20] C.J. Todaro, M.A. Easton, D. Qiu, D. Zhang, M.J. Bermingham, E.W. Lui, M. Brandt, D.H. Stjohn, M. Qian, Grain structure control during metal 3D printing by high-intensity ultrasound, Nat. Commun. 11 (2020) 142, https://doi.org/10.1038/s41467-019-13874-z.
[21] H. Ikehata, D. Mayweg, E. Jägle, Grain refinement of Fe–Ti alloys fabricated by laser powder bed fusion, Mater. Des. 204 (2021), https://doi.org/10.1016/j.matdes.2021.109665.
[22] N. Raghavan, R. Dehoff, S. Pannala, S. Simunovic, M. Kirka, J. Turner, N. Carlson, S.S. Babu, Numerical modeling of heat-transfer and the influence of process parameters on tailoring the grain morphology of IN718 in electron beam additive manufacturing, Acta Mater. 112 (2016) 303–314, https://doi.org/10.1016/j.actamat.2016.03.063.
[23] J. Mazumder, A. Schifferer, J. Choi, Direct materials deposition: designed macro and microstructure, Mater. Res. Innov. 3 (1999) 118–131, https://doi.org/10.1007/s100190050137.
[24] Y.L. Hu, X. Lin, X.F. Lu, S.Y. Zhang, H.O. Yang, L. Wei, W.D. Huang, Evolution of solidification microstructure and dynamic recrystallisation of Inconel 625 during laser solid forming process, J. Mater. Sci. 53 (2018) 15650–15666, https://doi.org/10.1007/s10853-018-2701-x.
[25] S. Bontha, N.W. Klingbeil, P.A. Kobryn, H.L. Fraser, Effects of process variables and size-scale on solidification microstructure in beam-based fabrication of bulky 3D structures, Mater. Sci. Eng. A 513–514 (2009) 311–318, https://doi.org/10.1016/j.msea.2009.02.019.
[26] S. Cadiou, M. Courtois, M. Carin, W. Berckmans, P. Le Masson, 3D heat transfer, fluid flow and electromagnetic model for cold metal transfer wire arc additive manufacturing (Cmt-Waam), Addit. Manuf. 36 (2020), https://doi.org/10.1016/j.addma.2020.101541.
[27] Q.K. Shen, X.D. Kong, X.Z. Chen, Fabrication of bulk Al-Co-Cr-Fe-Ni high-entropy alloy using combined cable wire arc additive manufacturing (CCW-AAM): microstructure and mechanical properties, J. Mater. Sci. Technol. 74 (2020) 136–142, https://doi.org/10.1016/j.jmst.2020.10.037.
[28] S.W. Williams, F. Martina, A.C. Addison, J. Ding, G. Pardal, P. Colegrove, Wire + arc additive manufacturing, Mater. Sci. Technol. 32 (2016) 641–647, https://doi.org/10.1179/1743284715y.0000000073.
[29] M. Dinovitzer, X. Chen, J. Laliberte, X. Huang, H. Frei, Effect of wire and arc additive manufacturing (WAAM) process parameters on bead geometry and microstructure, Addit. Manuf. 26 (2019) 138–146, https://doi.org/10.1016/j.addma.2018.12.013.
[30] M.J. Bermingham, D.H. Stjohn, J. Krynen, S. Tedman-Jones, M.S. Dargusch, Promoting the columnar to equiaxed transition and grain refinement of titanium alloys during additive manufacturing, Acta Mater. 168 (2019) 261–274, https://doi.org/10.1016/j.actamat.2019.02.020.
[31] M. Yamamoto, K. Shinozaki, K. Kadoi, D. Fujita, T. Inoue, M. Fukahori, Y. Kitahara, Development of Hot-wire Laser Welding Method for Lap Joint of Steel Sheet with Wide Gap, Q. J. Jpn. Weld. Soc. 29 (2011) 58s–61s, https://doi.org/10.2207/qjjws.29.58s.
[32] K.A. Mumtaz, N. Hopkinson, Selective Laser Melting of thin wall parts using pulse shaping, J. Mater. Process. Technol. 210 (2010) 279–287, https://doi.org/10.1016/j.jmatprotec.2009.09.011.
[33] C. Li, Y.B. Guo, J.B. Zhao, Interfacial phenomena and characteristics between the deposited material and substrate in selective laser melting Inconel 625, J. Mater. Process. Technol. 243 (2017) 269–281, https://doi.org/10.1016/j.jmatprotec.2016.12.033.
[34] K. Ando, J. Nishikawa, M.J.J.O.T.J.W.S. Inoue, Phenomena of the Molten Pool at High Current and High Speed MIG Welding. 40, 1971, pp. 307–311.
[35] J. Mazumder, A. Schifferer, J. Choi, Direct materials deposition: designed macro and microstructure, Mat. Res. Innov. 3 (2016) 118–131, https://doi.org/10.1007/s100190050137.
[36] T.A. Rodrigues, V.R. Duarte, D. Tomás, J.A. Avila, J.D. Escobar, E. Rossinyol, N. Schell, T.G. Santos, J.P. Oliveira, In-situ strengthening of a high strength low alloy steel during Wire and Arc Additive Manufacturing (WAAM), Addit. Manuf. 34 (2020), https://doi.org/10.1016/j.addma.2020.101200.
[37] S. Mereddy, M.J. Bermingham, D. Kent, A. Dehghan-Manshadi, D.H. Stjohn, M. S. Dargusch, Trace carbon addition to refine microstructure and enhance properties of additive-manufactured Ti-6Al-4V, Jom 70 (2018) 1670–1676, https://doi.org/10.1007/s11837-018-2994-x.
[38] A.S. Yildiz, K. Davut, B. Koc, O. Yilmaz, Wire arc additive manufacturing of high-strength low alloy steels: study of process parameters and their influence on the bead geometry and mechanical characteristics, Int. J. Adv. Manuf. Technol. 108 (2020) 3391–3404, https://doi.org/10.1007/s00170-020-05482-9.
[39] A.S. Yildiz, K. Davut, B. Koc, O. Yilmaz, Wire arc additive manufacturing of high-strength low alloy steels: study of process parameters and their influence on the bead geometry and mechanical characteristics, Int. J. Adv. Manuf. Technol. 108 (2020) 3391–3404, https://doi.org/10.1007/s00170-020-05482-9.
[40] M.S. Pham, B. Dovgyy, P.A. Hooper, C.M. Gourlay, A. Piglione, The role of side-branching in microstructure development in laser powder-bed fusion, Nat. Commun. 11 (2020) 749, https://doi.org/10.1038/s41467-020-14453-3.
[41] A.N.M. Tanvir, M.R.U. Ahsan, C. Ji, W. Hawkins, B. Bates, D.B. Kim, Heat treatment effects on Inconel 625 components fabricated by wire + arc additive manufacturing (WAAM)—part 1: microstructural characterization, Int. J. Adv. Manuf. Technol. 103 (2019) 3785–3798, https://doi.org/10.1007/s00170-019-03828-6.
[42] G. Ravi, N. Murugan, R. Arulmani, Microstructure and mechanical properties of Inconel-625 slab component fabricated by wire arc additive manufacturing, Mater. Sci. Technol. 36 (2020) 1785–1795, https://doi.org/10.1080/02670836.2020.1836737.
[43] S.H. Sun, T. Ishimoto, K. Hagihara, Y. Tsutsumi, T. Hanawa, T. Nakano, Excellent mechanical and corrosion properties of austenitic stainless steel with a unique crystallographic lamellar microstructure via selective laser melting, Scr. Mater. 159 (2019) 89–93, https://doi.org/10.1016/j.scriptamat.2018.09.017.
[44] Y.L. Hu, X. Lin, S.Y. Zhang, Y.M. Jiang, X.F. Lu, H.O. Yang, W.D. Huang, Effect of solution heat treatment on the microstructure and mechanical properties of Inconel 625 superalloy fabricated by laser solid forming, J. Alloy. Compd. 767 (2018) 330–344, https://doi.org/10.1016/j.jallcom.2018.07.087.
[45] S. Asgari, E. El-Danaf, S.R. Kalidindi, R.D. Doherty, Strain hardening regimes and microstructural evolution during large strain compression of low stacking fault energy fcc alloys that form deformation twins, Metall. Mater. Trans. A 28 (1997) 1781–1795, https://doi.org/10.1007/s11661-997-0109-3.
[46] U.F. Kocksa, H. Mecking, Physics and phenomenology of strain hardening: the FCC case, Prog. Mater. Sci. 48 (2003) 171–273, https://doi.org/10.1016/S0079-6425(02)00003-8.
[47] E. El-Danaf, S.R. Kalidindi, R.D. Doherty, Influence of grain size and stacking-fault energy on deformation twinning in fcc metals, Metall. Mater. Trans. A 30A (1999) 1223–1233, https://doi.org/10.1007/s11661-999-0272-9.
[48] Z. Sun, X. Tan, S.B. Tor, C.K. Chua, Simultaneously enhanced strength and ductility for 3D-printed stainless steel 316L by selective laser melting, NPG Asia Mater. 10 (2018) 127–136, https://doi.org/10.1038/s41427-018-0018-5.
[49] M. Yang, L. Wang, W. Yan, Phase-field modeling of grain evolution in additive manufacturing with addition of reinforcing particles, Addit. Manuf. (2021), 102286, https://doi.org/10.1016/j.addma.2021.102286.
[50] J.P. Oliveira, A.D. Lalonde, J. Ma, Processing parameters in laser powder bed fusion metal additive manufacturing, Mater. Des. 193 (2020), https://doi.org/10.1016/j.matdes.2020.108762.
[51] Y.Z. Li, A. Olmedilla, M. Zaloznik, J. Zollinger, L. Dembinski, A. Mathieu, Iop. Solidification microstructure during selective laser melting of Ni based superalloy: experiment and mesoscopic modelling[C].Joint Conference of 5th International Conference on Advances in Solidification Processes (ICASP) and 5th International Symposium on Cutting Edge of Computer Simulation of Solidification, Casting and Refining (CSSCR), 2019.
[52] Y.Z. Li, A. Olmedilla, M. Založnik, J. Zollinger, L. Dembinski, A. Mathieu, Solidification microstructure during selective laser melting of Ni based superalloy: experiment and mesoscopic modelling, IOP Conf. Ser.: Mater. Sci. Eng. 529 (2019), 012004, https://doi.org/10.1088/1757-899x/529/1/012004.
[53] A. Aggarwal, A. Chouhan, S. Patel, D.K. Yadav, A. Kumar, A.R. Vinod, K. G. Prashanth, N.P. Gurao, Role of impinging powder particles on melt pool hydrodynamics, thermal behaviour and microstructure in laser-assisted DED process: a particle-scale DEM – CFD – CA approach, Int. J. Heat Mass Transf. 158 (2020), 119989, https://doi.org/10.1016/j.ijheatmasstransfer.2020.119989.
[54] E. Orowan, Symposium on Internal Stresses in Metals and Alloys. Inst. Metals London, 1948, p.451.
[55] N. Hansen, Hall-Petch relation and boundary strengthening, Scr. Mater. 51 (2004) 801–806, https://doi.org/10.1016/j.scriptamat.2004.06.002.
[56] R.W. Kozar, A. Suzuki, W.W. Milligan, J.J. Schirra, M.F. Savage, T.M. Pollock, Strengthening mechanisms in polycrystalline multimodal Nickel-base superalloys, Metall. Mater. Trans. A 40 (2009) 1588–1603, https://doi.org/10.1007/s11661-009-9858-5.
[57] H. Mecking, U.F. Kocks, Kinetics of flow and strain-hardening, Acta Met. 29 (1981) 1865–1875, https://doi.org/10.1016/0001-6160(81)90112-7.
[58] K.M. Bertsch, G.M. De Bellefon, B. Kuehl, D.J. Thoma, Origin of dislocation structures in an additively manufactured austenitic stainless steel 316L, Acta Mater. 199 (2020) 19–33, https://doi.org/10.1016/j.actamat.2020.07.063.
[59] Y. Chew, Z.G. Zhu, F. Weng, S.B. Gao, F.L. Ng, B.Y. Lee, G.J. Bi, Microstructure and mechanical behavior of laser aided additive manufactured low carbon interstitial Fe49.5Mn30Co10Cr10C0.5 multicomponent alloy, J. Mater. Sci. Technol. 77 (2021) 38–46, https://doi.org/10.1016/j.jmst.2020.11.026.

[60] D.M. Collins, H.J. Stone, A modelling approach to yield strength optimisation in a nickel-base superalloy, Int. J. Plast. 54 (2014) 96–112, https://doi.org/10.1016/j.ijplas.2013.08.009.
[61] G.I. Taylor, Plastic strain in metals, J. Inst. Met. 62 (1938) 307–324.
[62] S.Y. Liu, H.Q. Li, C.X. Qin, R. Zong, X.Y. Fang, The effect of energy density on texture and mechanical anisotropy in selective laser melted Inconel 718, Mater. Des. 191 (2020), https://doi.org/10.1016/j.matdes.2020.108642.
[63] H.A. Roth, C.L. Davis, R.C. Thomson, Modeling solid solution strengthening in nickel alloys, Metall. Mater. Trans. A 28 (1997) 1329–1335, https://doi.org/10.1007/s11661-997-0268-2.
[64] K. Ma, H. Wen, T. Hu, T.D. Topping, D. Isheim, D.N. Seidman, E.J. Lavernia, J. M. Schoenung, Mechanical behavior and strengthening mechanisms in ultrafine grain precipitation-strengthened aluminum alloy, Acta Mater. 62 (2014) 141–155, https://doi.org/10.1016/j.actamat.2013.09.042.
[65] A.W. Thompson, Yielding in nickel as a function of grain or cell size, Acta Met. 23 (1975) 1337, https://doi.org/10.1016/0001-6160(75)90142-X.